ACS APPLIED MATERIALS & INTERFACES

www.acsami.org

Research Article

Synthesis and Characterization of the New $Li_{1+x}Al_{1+x}Si_{1-x}O_4$ (x = 0−0.25) Solid Electrolyte for Lithium-Ion Batteries

Je-Gwang Ryu, Ramkumar Balasubramaniam, Vanchiappan Aravindan,* Sangho Park,* Sung June Cho,* and Yun-Sung Lee*

Cite This: *ACS Appl. Mater. Interfaces* 2024, 16, 761−771

Read Online

ACCESS | Metrics & More | Article Recommendations | Supporting Information

ABSTRACT: A systematic study was performed to investigate the effect of the sintering temperature, sintering duration, and aluminum doping on the crystalline structure and ionic conductivity of the $Li_{1+x}Al_{1+x}Si_{1-x}O_4$ (LASO; x = 0−0.25) solid electrolyte. There was a strong indication that an increase in the sintering temperature and sintering time increased the ionic conductivity of the electrolyte. In particular, the doping concentration and composition ratio ($Li_{1+x}Al_{1+x}Si_{1-x}O_4$; x = 0−0.25) were found to be crucial factors for achieving high ionic conductivity. The sintering time of 18 h and lithium concentration influenced the lattice parameters of the LASO electrolyte, resulting in a significant improvement in ionic conductivity from 2.11 × 10^{-6} (for pristine LASO) to 1.07 × 10^{-5} S cm^{-1}. An increase in the lithium concentration affected the stoichiometry, and it facilitated a smoother Li-ion transfer process since lithium served as an ion-conducting bridge between LASO grains.

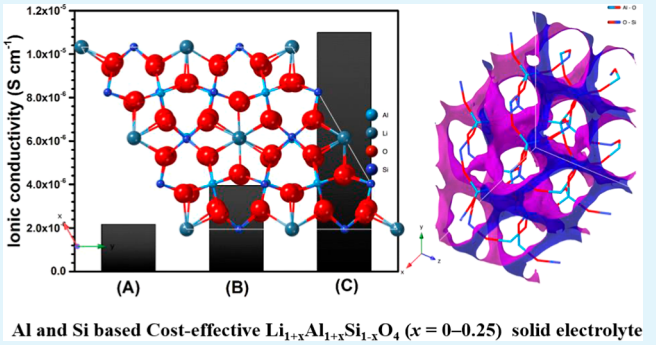

Al and Si based Cost-effective $Li_{1+x}Al_{1+x}Si_{1-x}O_4$ (x = 0–0.25) solid electrolyte

KEYWORDS: *solid electrolyte, sintering temperature, doping effect, lattice parameter, lithium ionic conductivity*

1. INTRODUCTION

The rapid development of the world economy at the beginning of the twentieth century changed the lifestyle of people; petrol and diesel vehicles became essential parts of life. The limited availability of fossil fuel resources and the formation of CO_2 and harmful substances during their combustion.[1,2] Accordingly, this prompted research into alternative green energy sources, such as solar and wind energy. However, since solar and wind energy are intermittent, storage devices are required to store power produced from these renewable sources. Consequently, there is a need for rechargeable devices, such as batteries. Among secondary batteries (Pb-acid, Ni−Cd, Ni-MH batteries), lithium-ion batteries (LIBs) have become popular owing to their higher operating potential and specific capacity, which make them suitable for use as electrochemical energy storage devices.[3] However, the energy density of the current state-of-the-art LIBs is just over 200 W h kg^{-1}, which is insufficient to overcome the futuristic energy crisis.[3,4]

Li metal-based batteries provide higher energy density than LIBs, but they have drawbacks: the formation of Li dendrites, an unstable solid electrolyte (SE) interphase, dead lithium, and related safety issues.[4] Their commercial applications are hence limited, and research on the development of strategies to overcome these drawbacks is being conducted. Among the best strategies is the introduction of SEs between the electrodes. The high mechanical stability of SEs can suppress Li dendrite formation.[5] Generally, a good SE should have high ionic conductivity and reasonable critical current density to suppress Li dendrite formation across the Li/electrolyte interface, negligible electronic conductivity, a wide electrochemical stability window, and good chemical compatibility with the electrode (cathode and anode) materials.[6−9] Furthermore, it should have high stability when exposed to air and H_2O under ambient temperature conditions.[7] Unlike polymer electrolytes, ceramic electrolytes have high Li-ion conductivity, high ionic transfer number, high electrochemical stability, and excellent thermal stability.[10−15]

Generally, on the basis of their chemical nature, ceramic SEs are classified as (i) oxide, (ii) sulfide, and (iii) nitride SEs. Oxide ceramics are considered superior to other SEs because of their high Li-ion conductivity and excellent electrochemical stability with cathode materials and with the Li metal anode.[8,9,12] The most commonly used oxide SEs are perovskite ($Li_xLa_{(2-x)/3}TiO_3$), NASICON ($Li_{1+x}M_{2-x}^{4+}2M'_x(PO_4)_3$, where M = Ti or Ge, M' = Al), and garnet and its derivatives

Received: October 11, 2023
Revised: November 30, 2023
Accepted: November 30, 2023
Published: December 18, 2023

($Li_{7-x}La_3Zr_{1-x}MO_{12}$, where M = Nb or Ta; $Li_{7-x}Y_xLa_3Zr_2O_{12}$, where Y= Al or Ga).[6,8,9,12,13,16−21] Most of the oxide SEs are sintered with rare earth and expensive materials at high temperatures (>1000 °C) to reduce the grain boundary resistance. Further, elements such as Ti and Ge are easily reduced to a lower valence state during the electrochemical operation of the battery.[22−24] Compared with other structures, the garnet phase is stable, but its poor air stability is the main impediment to its practical application. The surface of the material easily reacts with moisture (H_2O) to form Li_2CO_3, which impedes Li-ion transfer and eventually increases the surface resistance of the material.[25,26]

Considering these points, we used earth-abundant elemental materials for SE research. In particular, from industrial and foresight viewpoints, cost-effective elements are a good choice for SE preparation. Hence, we used aluminum (Al, 7.5%) and silicon (Si, 25.7%) earth-abundant framework cation materials to prepare Li-ion conductive SEs.[27,28] Based on the reported work, the $LiAlSiO_4$ crystal structure contains the SiO_4 and AlO_4 tetrahedra and bridging oxygens, with Li-ions occupying interstitial sites.[29,30] The reported $LiAlSiO_4$ exhibits reasonable ionic conductivity, in which the Li-ion conduction is on 1-D channels along the *c*-axis.[29] Several techniques have been employed to prepare the $LiAlSiO_4$ SE, including atomic layer deposition (ALD), the magnetron sputtering method, and the sol-gel method.[29,31,32] Nevertheless, the thin-film SE battery costs were high, and the process was difficult. Herein, we prepared the $LiAlSiO_4$-based SEs by a simple sol−gel method because of its scalability and economical compared to other methods. Generally, more Li-ions are essential for a greater ionic conductivity in the electrolyte; therefore, the incorporation of additional Al atoms is also necessary. Here, we improved the ionic conductivity of SE by increasing the doping concentration of both Al and Li atoms. Additionally, we intensively studied the physicochemical and electrochemical properties of $Li_{1+x}Al_{1+x}Si_{1-x}O_4$ (X = 0−0.25) (LASO) SEs. The effect of different sintering temperatures on the hexagonal structure formation in the sintering process was evaluated. The variation of the relative density and conductivity of the SE with the sintering duration was investigated. The main advantage of the LASO SE is its elemental selection and sintering temperature (<1000 °C).

2. EXPERIMENTAL SECTION

2.1. Preparation of LASO SEs. $Li_{1+x}Al_{1+x}Si_{1-x}O_4$ (LASO; x = 0−0.25) SEs were synthesized via the sol−gel method. Stoichiometric amounts of $LiNO_3$, $Al(NO_3)_3{\cdot}9H_2O$, and $Si(OC_2H_5)_4$, which were the precursor materials, were used for the synthesis. Initially, $LiNO_3$, $Al(NO_3)_3{\cdot}9H_2O$, and $Si(OC_2H_5)_4$ were dissolved in distilled water, and the solution was stirred for 12 h. The precursor solution was then heated at 120 °C overnight to evaporate the water. The resultant powder was ground and then calcined at 400 °C for 6 h in an air atmosphere. Subsequently, the powders were ground and then pressed into pellets at a 100 MPa pressure. Finally, the pellets were sintered at 650−850 °C for 6 h in an air atmosphere. The LASO pellets were used for further physicochemical and electrochemical investigations.

2.2. Material and Electrochemical Characterizations of LASO SEs. The LASO SE crystal structure and lattice parameters were obtained through geometry optimization performed using density functional theory (DFT) simulation implemented in the Quantum ESPRESSO package (Version 7.2).[33] Lithium aluminosilicate crystal structure databases were obtained from the Materials Project Database (https://materialsproject.org/). The following analysis was performed to analyze the physicochemical properties of the synthesized LASO (x = 0−0.25). High-resolution X-ray diffraction (XRD)(D/Max Ultima III, Rigaku, Japan; 40 kV/40 mA) was used to investigate the LASO-based SE crystal structure. XRD data were obtained in the range of 10−80°, with a step size of 0.02°. Field-emission scanning electron microscopy (FE-SEM; Zeiss, Germany) was used to observe the surface morphology and determine the particle size of the LASO SE pellets and powder. Before sintering, thermogravimetric analysis (TGA; TGA-50, Shimadzu, Japan) was performed to determine the thermal behavior of the sample by the sol−gel method and to ascertain the optimal sintering temperature. Thermal analysis was performed up to 1000 °C at a heating rate of 10 °C min^{-1} in an air atmosphere. Inductively coupled plasma optical emission spectroscopy (ICP-OES; OPTIMA 8300, PerkinElmer) was performed to determine the stoichiometry of the $Li_{1+x}Al_{1+x}Si_{1-x}O_4$ (x = 0−−0.25) SEs for changes in the composition. The ionic conductivity of the LASO electrolyte was measured with a 4284A precision LCR meter (HEWLETT PACKARD). A pellet with a thickness of about 1.76 mm and a diameter of 10 mm was used for the ionic conductivity measurements. Pt was sputtered on both sides of the pellet to form the Pt/LASO/Pt cells. Electrochemical impedance was obtained for an AC amplitude (10 mV) in the frequency range of 1 MHz to 25 Hz at a temperature of 25 °C. The ionic conductivity was calculated using the formula: $\sigma = d/(A \times R)$, where d and A are the thickness and surface area of the pellet, respectively, and R is the total resistance value obtained by applying electrochemical impedance spectra.

The Li//LASO//Li symmetric cell was also constructed using a 2032 coin-cell, and the galvanostatic charge and discharge performance was studied at a current density of 0.1 mA cm^{-2}. The $LiFePO_4$ (LFP) cathode was prepared by a solution casting method. LFP (MTI Corporation), Super-P, and PVDF binder (7:2:1 ratio) were ground in a mortar and then mixed with the NMP solvent. Then, the slurry was cast on an Al foil current collector and the electrode was vacuum-dried at 120 °C overnight. In the cathode composite, the LFP loading mass was calculated to be ∼2 mg cm^{-2}. The solid-state battery is constructed of the LFP cathode and Li metal as the anode separated by the LASO pellet. Additionally, we added 10 μL of a liquid electrolyte (1 M $LiPF_6$ in EC/DMC) in the electrode and electrolyte interface to improve the electrochemical performance of the aforesaid solid-state battery. The charge and discharge performance of the solid-state battery was tested at 25 °C.

3. RESULTS AND DISCUSSION

3.1. Theoretical Studies of LASO SEs. There are several lithium aluminosilicates that can be prepared experimentally, and they can be found in the Materials Project Database (https://materialsproject.org/); the crystal structure data of LASO SE is listed in Table 1. The corresponding crystal structure is shown in Figure 1. Aluminosilicates containing a high proportion of lithium can be effective ion conductors; they have a small band gap and many mobile Li-ions.[34] The Nernst−Einstein equation was used along with molecular dynamics simulations performed using a large-scale atomic/molecular massively parallel simulator and the single-atom

https://doi.org/10.1021/acsami.3c15221
ACS Appl. Mater. Interfaces 2024, 16, 761−771

Table 1. Experimentally Observed Lithium Aluminosilicate Analogues Obtained from the Materials Project Database (https://materialsproject.org/)

ID	mp-558713
formula	$LiAlSiO_4$
crystal system	hexagonal
space group	P_{6_222}
band gap (eV)	4.51

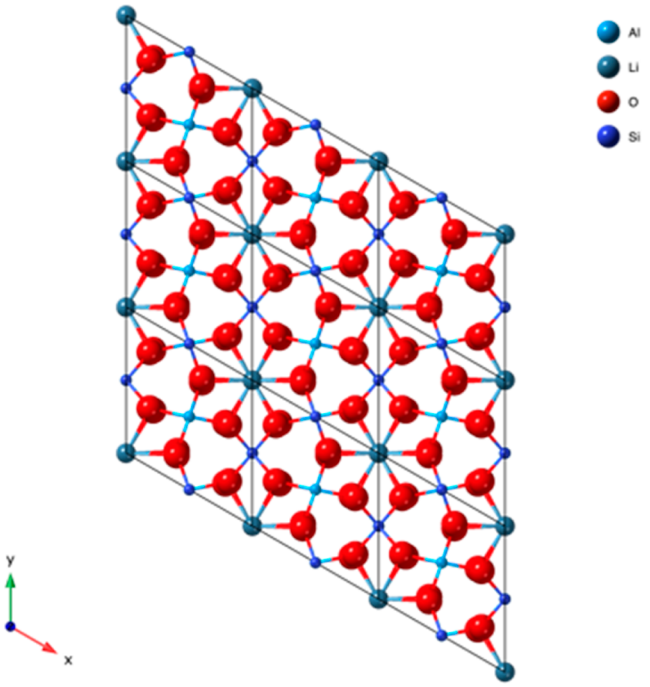

Figure 1. Crystal structures of lithium aluminosilicates: $LiAlSiO_4$.

Table 2. Diffusion Coefficient of the Li^+ Ion in and the Conductivity of Li^+ Aluminosilicates Obtained from the MDS[a]

	D (10^{-2} Å^2 s^{-1})	σ (10^{-3} S cm^{-1})
$LiAlSiO_4$	11.37	7.69

[a]The force field was produced using the neural network potential for $LiAlSiO_4$.

neural network potential (SANNP) to determine the diffusion coefficient and ion conductivity.[35−38] The SANNP for $LiAlSiO_4$ was generated by first creating an initial force field on the basis of a small training data set and then training the neural network. The training data set consisted of 1000 structures generated by randomly displacing the atomic coordinates by 0.1−0.2 Å and performing SCF calculations on each set of coordinates using Quantum ESPRESSO with ultrasoft pseudopotentials, a cutoff energy of 40 Ry, and k-point sampling at Γ points.[33] Optimized force fields were then used to perform molecular dynamics (MD) simulations in an NVT ensemble with T = 300 K, Δt = 0.5 fs, a simulation time of 500 ps, and a 378-atom supercell model (2 × 2 × 2). The diffusion coefficient was obtained from the slope of the mean square displacement (MSD) of around 0.5 ns.

Figure S1 shows MSDs obtained from MD simulations for lithium aluminosilicates. $LiAlSiO_4$ showed a significant MSD and could be considered to have highly mobile Li-ions. By

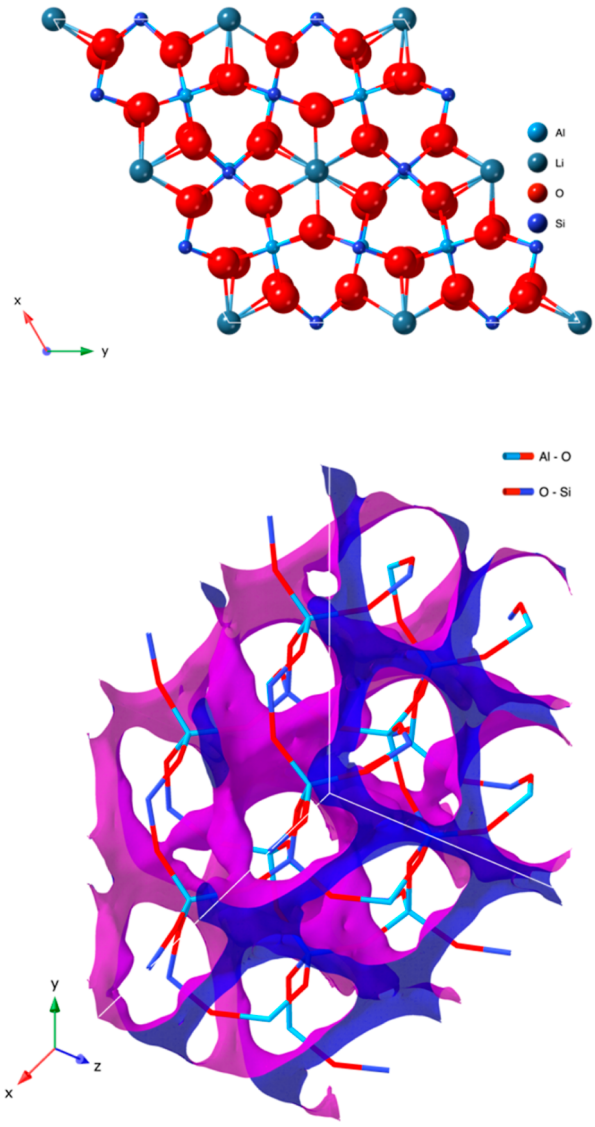

Figure 2. Crystal structure of the optimized $LiAlSiO_4$ and the corresponding channel structure.

using the MSD data as a function of time, we could calculate the diffusion coefficient and the corresponding conductivity could be readily obtained (Table 2). In a crystal with no grain boundary, $LiAlSiO_4$ showed the highest conductivity, as expected. The radial distribution function of Li in the crystal system is presented in Figure S2. Li interacts with Al and Si at the same distances, and the separation of Li−Li pairs is expected to be 2.5−3.0 Å, suggesting cooperative migration of Li in the channel, as illustrated in Figure 2, where the Li path is shown in blue.

3.2. Optimization of Sintering Temperature of the LASO Electrolyte. *3.2.1. X-ray Diffraction Studies and Electrochemical Characterization of the $LiAlSiO_4$ SE through Sintering Temperature Optimization.* The sintering process is an important process in SE preparation that can affect the structural properties of the electrolyte, such as increasing the relative density and reducing the bulk and grain boundary resistance.[39] Therefore, the optimization of the sintering temperature and sintering time and choosing an appropriate sintering atmosphere are important to obtain the target structure. It is also necessary to prevent lithium loss during

https://doi.org/10.1021/acsami.3c15221
ACS Appl. Mater. Interfaces 2024, 16, 761−771

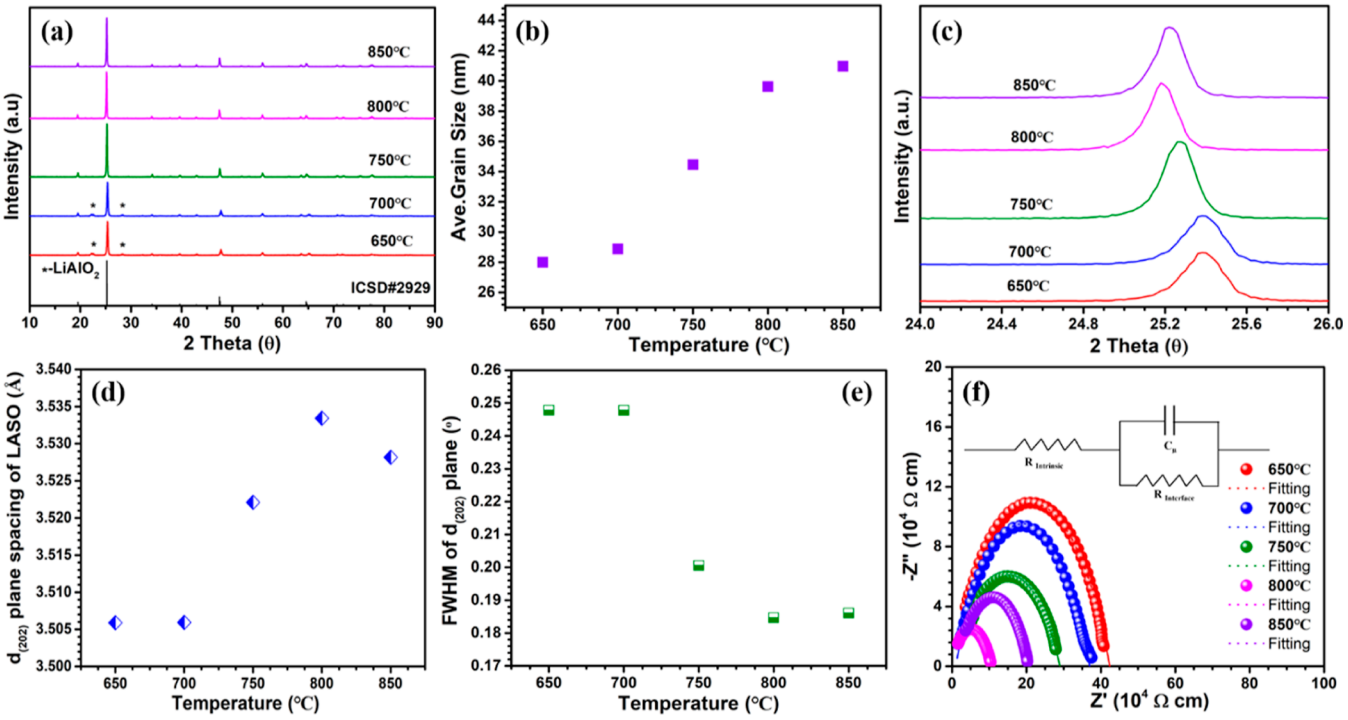

Figure 3. (a) XRD patterns of the LASO material sintered at different temperatures and (b) a plot of the sintering temperature (°C) versus the average grain size (nm) of the LASO SEs. (c) XRD patterns of the $d_{(202)}$ plane for different sintering temperatures. (d) Plot of the temperature versus the $d_{(202)}$ plane spacing of LASO SEs (Å). (e) Variation of the fwhm of the $d_{(202)}$ plane of the SEs with the sintering temperature. (f) EIS curves of $LiAlSiO_4$ materials sintered at different temperatures.

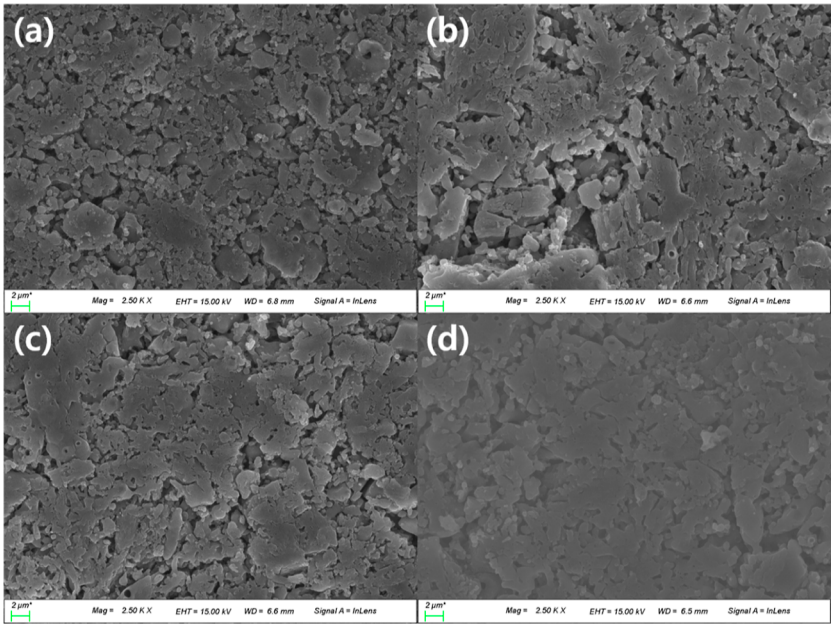

Figure 4. SEM images of $LiAlSiO_4$ materials sintered at (a) 650, (b) 700, (c) 750, and (d) 800 °C.

sintering and to optimize the composition of the ceramic electrolyte. In this work, the precursor was calcined at 400 °C for 6 h in an air atmosphere to determine the optimal synthesis conditions of the LASO electrolyte. Finally, pellets of lithium aluminosilicates were sintered at different temperatures in the range of 650−800 °C for 6 h in an air atmosphere at intervals of 50 °C.

XRD analysis was performed to ascertain the structural properties of the electrolytes sintered at various temperatures, and the XRD patterns obtained are shown in Figure 3a. Clearly, the intensity of the diffraction peaks of LASO electrolytes increased with the sintering temperature. The sharp peaks are attributed to the enhancement of the crystallinity, which is important for improving the electrochemical performance of the LASO SE.[40] The XRD patterns of electrolytes sintered at temperatures of 750 °C or higher matched that of the single-phase $LiAlSiO_4$ phase (ICSD: 2929), but the electrolytes sintered at 700 °C or lower

https://doi.org/10.1021/acsami.3c15221
ACS Appl. Mater. Interfaces 2024, 16, 761−771

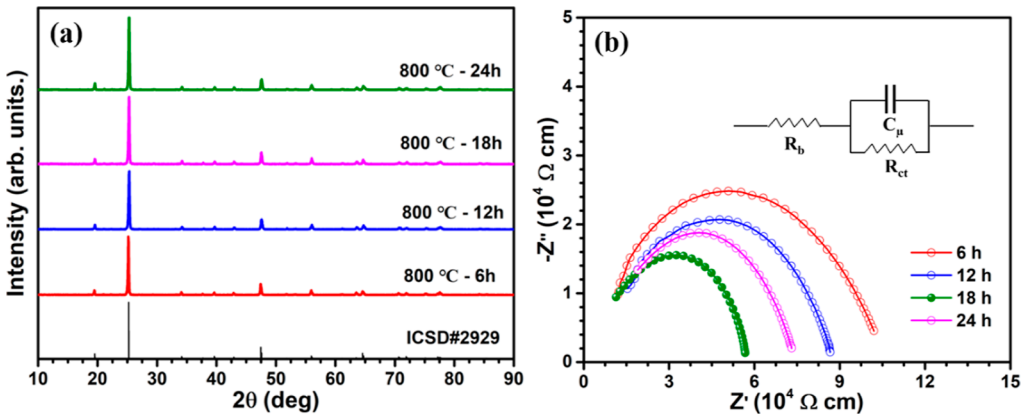

Figure 5. (a) XRD patterns of $LiAlSiO_4$ materials sintered at 800 °C for different durations. (b) EIS curves of $LiAlSiO_4$ materials sintered for different durations.

Table 3. Comparison of Lattice Parameters for Different Sintering Durations

time	*a* (Å)	*b* (Å)	*c* (Å)	*V* (Å^3)
6 h	10.4742	10.4742	11.1325	1057.7062
12 h	10.4768	10.4768	11.1538	1060.2561
18 h	10.4792	10.4792	11.1652	1061.8261

Table 4. Lattice Parameters of Lithium Aluminosilicates Obtained from Le Bail Refinement of X-ray Diffraction Data

x in $Li_{1+x}Al_{1+x}Si_{1-x}O_2$	*a* (Å)	*c* (Å)	volume (Å^3)
0	10.4856	11.1898	2770.201
0.05	10.4939	11.1649	2768.422
0.15	10.4926	11.1785	2771.126
0.25	10.4979	11.1627	2769.997
0[a]	10.5177	11.3316	2822.518

[a]The Lattice Parameters were Obtained through Geometry Optimization Using DFT Simulation Implemented in the Quantum ESPRESSO Package.

Table 5. ICP-OES Analysis Results of the $Li_{1+x}Al_{1+x}Si_{1-x}O_4$ (x = 0–0.25, LASO) Materials

x	Li/O	Al/O	Si/O	formula
0	1.01	1.0	0.99	$Li_{1.01}Al_{1.02}Si_{0.99}O_4$
0.05	1.06	1.05	0.94	$Li_{1.06}Al_{1.05}Si_{0.94}O_4$
0.15	1.17	1.16	0.84	$Li_{1.17}Al_{1.16}Si_{0.84}O_4$
0.25	1.26	1.25	0.76	$Li_{1.26}Al_{1.25}Si_{0.76}O_4$

temperatures contained trace amounts of $LiAlO_2$ impurities.[41−43] These results confirmed that oxygen and silicon atoms combined during sintering at low temperatures (≤700 °C), which is undesirable. When pellets were sintered at a temperature of 850 °C or higher, the crystallinity of the electrolyte decreased because of the formation of a lithium-deficient phase, which indicated lithium volatilization at high temperatures. Therefore, we identified 800 °C as the optimum temperature to obtain the pure $LiAlSiO_4$ phase.

Figure 3b shows a plot of the temperature versus the average grain (crystallite) size of the LASO SEs. The Debye−Scherrer equation was used to calculate the average grain size of the electrolyte[5,39]

$$D = \frac{K \cdot \lambda}{\text{fwhm}(2\theta) \cdot \cos(\theta)}$$

where the Scherrer constant K = 0.9, the X-ray wavelength λ = 0.15418 nm, β is the full width at half-maximum (fwhm), and θ is Bragg's diffraction angle. The sintering temperature is a major factor determining the grain size of the LASO-based SEs. The average grain sizes of LASO-650, LASO-700, LASO-750, LASO-800, and LASO-850 were 28, 29, 34, 40, and 41 nm, respectively. It is noteworthy that the average grain size increased with the sintering temperature. An increase in the sintering temperature leads to the migration of grain

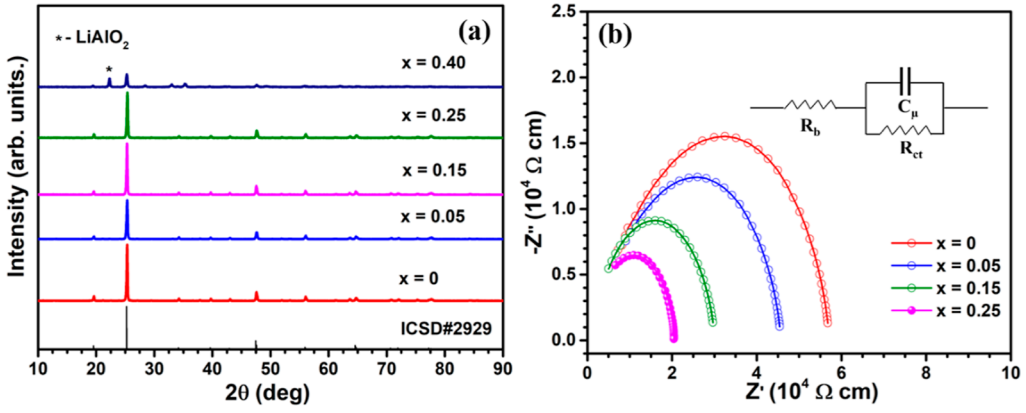

Figure 6. (a) XRD patterns and (b) EIS curves of $Li_{1+x}Al_{1+x}Si_{1-x}O_4$ (x = 0, 0.05, 0.15, 0.25, 0.4) SEs.

https://doi.org/10.1021/acsami.3c15221
ACS Appl. Mater. Interfaces 2024, 16, 761−771

Table 6. Comparison of Ionic Conductivities of Previously Reported LASO SEs and the $Li_{1+x}Al_{1+x}Si_{1-x}O_4$ (x = 0−0.25, LASO) SEs of the Current Study[a]

electrolytes	preparation method, electrolyte type and thickness	ionic conductivity and synthesis temperature	references
β-eucryptite $LiAlSiO_4$ thin-film SEs	ALD of $LiAlSiO_4$ thin-film ~20 and 48 nm	1.2×10^{-7} S cm^{-1} (25 °C)—rapid thermal annealing at 900 °C	29
$LiAlSiO_4$ thin film	magnetron sputtering method—thin-film ~60 nm	2.7×10^{-8} S cm^{-1} (25 °C)—annealed at 900 °C	31
PEO + LiTFSI + $LiAlSiO_4$	sol−gel method—composite polymer SSE—100−130 μm	1.62×10^{-4} S cm^{-1} (40 °C)—sintered at 900 °C	32
$Li_{1+x}Al_{1+x}Si_{1-x}O_4$ (x = 0−0.25) ceramic SE	sol−gel method—ceramic pellet ~1.76 mm	3.95×10^{-6} S cm^{-1} (x = 0) and 1.1×10^{-5} S cm^{-1} (x = 0.25) (25 °C)—sintered at 800 °C	our work

[a](ALD—atomic layer deposition method, PEO—poly(ethylene oxide), LiTFSI—lithium bis(trifluoromethanesulfonyl)imide).

boundaries, and grain growth depends strongly on the sintering temperature.[44,45]

Electrochemical impedance spectroscopy (EIS) was used to analyze the LASO SE prepared at different sintering temperatures, and the EIS results are shown in Figure 3f. The resistance decreased as the sintered temperature increased (>650 °C). From these data, the total ionic conductivity of the LASO pellet sintered at 800 °C was calculated to be 2.11×10^{-6} S cm^{-1} (25 °C). This high ionic conductivity is likely to be associated with crystallographic characteristics, such as the interplanar spacing distance (d) and crystallinity of the sintered LASO pellet. The comparisons of ionic conductivities of the $LiAlSiO_4$ SE for different sintering temperatures are listed in Table S1. Figure 3c,d shows a comparison of the diffraction patterns and d spacing for different sintering temperatures. Apparently, the d spacing increased when the material was maintained at a high temperature for a long duration.[46] This is due to thermal expansion because the thermal expansion coefficient of the crystal for the direction along the mutual space in the crystal structure varies with temperature. Therefore, it was concluded that the higher sintering temperature induced more d spacing by thermal expansion.

In ceramic SEs, high crystallinity of the material is essential for fast Li-ion conduction. The crystallinity of electrolytes can be calculated from the fwhm of the (202) major peak, which can be determined from XRD patterns. Figure 3e shows the relationship between the fwhm and the sintering temperature. The crystallinity is inversely related to the fwhm of the XRD peak.[39] For the sintering temperature of 650 °C, the (202) peak was broad and had a high fwhm of 0.25°, indicating poor crystallinity. The crystallinity improved significantly at 800 °C and became saturated. The highest crystallinity was attained at 800 °C, and LASO showed a clear sharp peak with the smallest fwhm (0.18°). However, the resistance of the sample sintered at 850 °C was large, and it was due to the formation of a Li-deficient phase as a result of lithium volatilization at this high temperature. Hence, it was confirmed that the pellet sintered at 800 °C in which $LiAlO_2$ impurities were absent (indicated by XRD results) had high ionic conductivity. Hence, the optimum sintering temperature for preparing $LiAlSiO_4$-based SEs was identified as 800 °C.

3.2.2. Morphological Results. Figure 4 shows FE-SEM analysis results of $LiAlSiO_4$ pellets sintered at different temperatures in the range of 650−800 °C. With an increase in the sintering temperature from 650 to 800 °C, there was no significant change in the morphology, but the particle size increased and the porosity between particles decreased, which indicated that the pellet's density increased. The relative density of the pellet continuously increased to around 65% as the sintering temperature increased from 650 to 800 °C. Frank Tietz's group[39] found that increasing the density of an $Li_{1.5}Al_{0.5}Ti_{1.5}(PO_4)_3$ oxide-based SE increased the SE's ionic conductivity. As the sintering temperature increases, the particles expand, which results in a decrease in the porosity and an increase in the pellet density. It was inferred that the increase in the pellet density promoted smooth Li-ion transfer between particles and eventually increased the total Li-ion conductivity. The surface morphology of the synthesized $LiAlSiO_4$ sintered at 800 °C is shown in Figure S3. The synthesized powder was coarse with a particle size of ~9 μm.

3.3. Structural and Electrochemical Characterization of the $LiAlSiO_4$ SE through Sintering Time Optimization. To optimize the sintering time, we sintered LASO pellets

https://doi.org/10.1021/acsami.3c15221
ACS Appl. Mater. Interfaces 2024, 16, 761−771

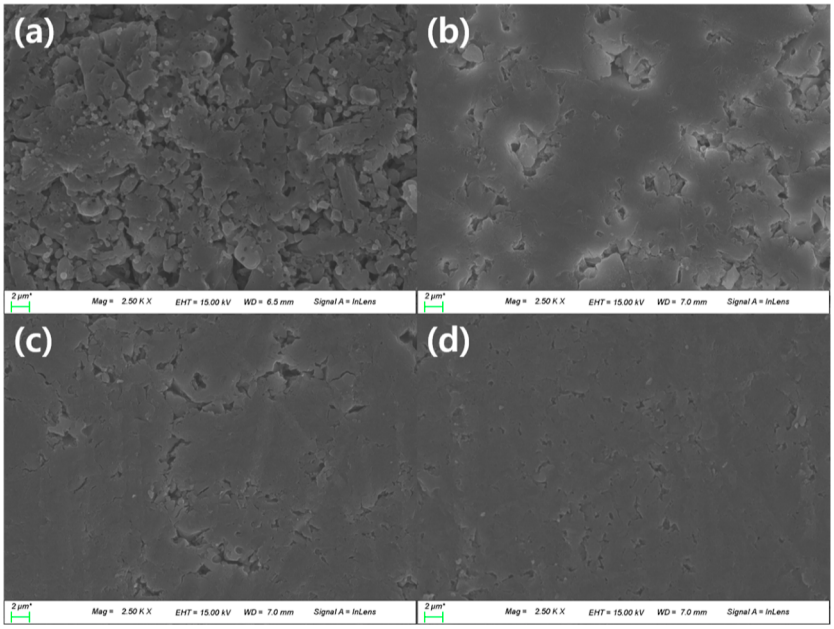

Figure 7. FE-SEM images of $Li_{1+x}Al_{1+x}Si_{1-x}O_4$ materials with (a) $x = 0$, (b) $x = 0.05$, (c) $x = 0.15$, and (d) $x = 0.25$.

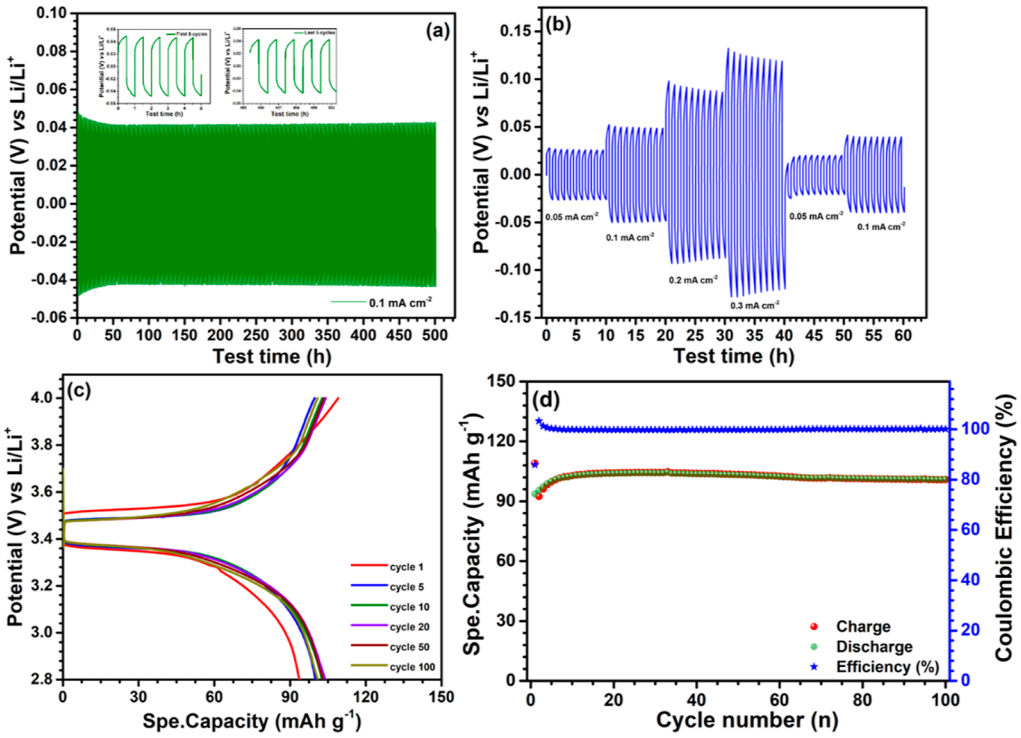

Figure 8. Galvanostatic charge−discharge performance for the Li//$Li_{1+x}Al_{1+x}Si_{1-x}O_4$ ($x = 0.25$)//Li symmetric cell at a (a) 0.1 mA cm^{-2} current density. (b) Different (0.05, 0.1, 0.2, and 0.3 mA cm^{-2}) current densities. (c) Galvanostatic charge−discharge performance for selected cycles. (d) Cycle life of the Li//$Li_{1+x}Al_{1+x}Si_{1-x}O_4$ ($x = 0.25$)//LFP cell at a rate of 0.2 C at 25 °C.

at 800 °C for different durations in the range of 6 to 24 h, at intervals of 6 h. Furthermore, the dependence of the structure and electrochemical properties of $LiAlSiO_4$ SEs on the sintering time was examined. Figure 5a shows the XRD patterns of the LASO electrolyte sintered at 800 °C for different durations. The XRD peaks are sharp, confirming its crystalline nature, and no secondary phase was formed in the electrolyte. The electrochemical data in Figure 5b confirm that the total resistance value of the $LiAlSiO_4$ SEs decreased as the sintering time increased beyond 6 h. In particular, the SE sintered for 18 h had the smallest total resistance, namely, 57.5 kΩ. For a longer sintering time, the resistance value tended to increase by 74.5 kΩ. The comparisons of ionic conductivity of the $LiAlSiO_4$ SE for different sintering times are listed in Table S2.

To determine the reason for the drop in the resistance of $LiAlSiO_4$-based SEs sintered at 800 °C for a longer duration (>6 h), the lattice parameters were calculated; the lattice

https://doi.org/10.1021/acsami.3c15221
ACS Appl. Mater. Interfaces 2024, 16, 761−771

Table 7. Capacity Retention and Capacity Fade Rate of the Li//Li1+xAl1+xSi1−xO4 (x = 0.25)//LFP Cell at the 0.2 C Rate

cycle	capacity (mA h g^{-1})	capacity retention (%)	capacity fade rate (%)
1	94		
20	104		
50	103	99	0.033
100	101	97	0.037

parameters are tabulated in Table 3. Peak shifts were observed and confirmed in the XRD pattern. According to Bragg's law ($n\lambda = 2d_{hkl} \sin\theta$), the d_{hkl} interplanar distance increases when 2θ decreases.[5,47] Therefore, the shift in the XRD pattern indicated a change in the lattice parameters and volume variations. Accordingly, it was considered that the volume of the bottleneck would expand and that the ionic conductivity would increase eventually. The lattice constants of the $LiAlSiO_4$ SEs sintered for 6 h were $a = b = 10.4742$ Å and $c = 11.1325$ Å, whereas those for 18 h sintering were larger ($a = b = 10.4792$ Å and $c = 11.1652$ Å). The lattice parameters of the $LiAlSiO_4$ SE and the unit cell volume increased with the sintering duration. The increase in the cell volume implies that lithium ions can diffuse more easily through the electrolyte and that the volume of the bottleneck can be increased to enhance Li-ion conduction.

3.4. Optimization of Composition $Li_{1+x}Al_{1+x}Si_{1-x}O_4$ (x = 0, 0.05, 0.15, 0.25, 0.4) SEs. *3.4.1. Theoretical Studies of $Li_{1+x}Al_{1+x}Si_{1-x}O_4$ (LASO) SEs.* The change in lattice parameters as a function of the Li and Al content of the sample is presented in Table 4, where the lattice parameters were obtained through Le Bail refinement of the XRD data.[48] However, the obtained lattice parameters and cell volume were smaller than those obtained from the optimized structure by using the Quantum ESPRESSO package (Version 7.2) with ultrasoft pseudopotential, where the cutoff for the wave function and charge were 40 and 360 Ry, respectively, and the generalized gradient approximation with the Perdew−Burke−Ernzerhof exchange functional and DFT-D3 van der Waals dispersion corrections were used.[49,50] An increase in the Al content increased the lattice parameter *a*, while *c* decreased, causing the cell volume to remain constant. These results suggest the progressive substitution of Al into the Si position, while the Li−Li interaction may increase the electrostatic repulsion. The electrostatic repulsion increases the ionic conductivity of the electrolyte.

3.4.2. Structural and Morphological Analysis of $Li_{1+x}Al_{1+x}Si_{1-x}O_4$ (LASO) SEs. On the basis of theoretical studies, we prepared $Li_{1+x}Al_{1+x}Si_{1-x}O_4$ ($x = 0-0.25$) (LASO) SEs with different Li concentrations. XRD analysis was used to study the crystal structure of the prepared $Li_{1+x}Al_{1+x}Si_{1-x}O_4$ ($x = 0-0.4$) SEs, and the results are shown in Figure 6a. The results confirmed that a hexagonal phase structure was formed without any secondary phase formation for the composition range of $x = 0$ to 0.25. A higher composition ($x = 0.4$) XRD pattern showed the presence of $LiAlO_2$ as an impurity phase, formed because of the poor combination of lithium and aluminum with oxygen, leading to a decrease in the silicon ratio in the synthesized $Li_{1+x}Al_{1+x}Si_{1-x}O_4$ ($x = 0.4$) SEs.[51] Table 5 shows the results of ICP-OES, which was performed to determine the actual stoichiometric ratio of the $Li_{1+x}Al_{1+x}Si_{1-x}O_4$ ($x = 0-0.25$) SEs. The ICP-OES analysis was performed after pretreatment with aqua regia. It was confirmed that the calculated stoichiometric ratios were accurate for the four different compositions prepared.

3.4.3. Analysis of Electrochemical Properties of the $Li_{1+x}Al_{1+x}Si_{1-x}O_4$ SE. EIS was performed to measure the resistance of $Li_{1+x}Al_{1+x}Si_{1-x}O_4$ ($x = 0-0.4$) SEs with various compositions, and the results are shown in Figure 6b. As the Li ratio increased, the resistance value of the electrolyte decreased. The charge-transfer resistance value of the $LiAlSiO_4$ SE was about 57.5 kΩ, but that of $Li_{1.25}Al_{1.25}Si_{0.75}O_4$ decreased to 20.9 kΩ. This confirmed that the substitution of Li composition decreased the resistance value of the electrolyte. The $Li_{1.25}Al_{1.25}Si_{0.75}O_4$ SE easily formed a hexagonal structure through substitution, with increased Li content and faster movement of Li ions. In summary, the ionic conductivity of the $LiAlSiO_4$ SE sintered at 800 °C for 18 h was 3.89×10^{-6} S cm^{-1}, and the ionic conductivity of Li-substituted $Li_{1.25}Al_{1.25}Si_{0.75}O_4$ SE was 1.07×10^{-5} S cm^{-1}. The comparison of intrinsic and interface ionic conductivity of $Li_{1+x}Al_{1+x}Si_{1-x}O_4$ ($x = 0-0.40$) SEs are listed in Table S3. In Table 6, we compare our $Li_{1+x}Al_{1+x}Si_{1-x}O_4$ ($x = 0-0.25$) SE ionic conductivity with previously reported conductivities.[29,31,32] Additionally, Figure 7b shows the EIS profile of the $Li_{1.4}Al_{1.4}Si_{0.6}O_4$ SE and the total resistance of the $Li_{1.4}Al_{1.4}Si_{0.6}O_4$ SE is increased to 2560 K. This confirms the existence of $LiAlO_2$ impurity and eventually increases the resistance value of the electrolyte. Table S3 shows a comparison of the ionic conductivity of the $Li_{1+x}Al_{1+x}Si_{1-x}O_4$ ($x = 0-0.4$, LASO) SEs. The intrinsic and interface ionic conductivities of the $Li_{1.4}Al_{1.4}Si_{0.6}O_4$ SE were 3.379×10^{-7} and 8.99×10^{-9} S cm^{-1}. Consequently, it confirmed the impurity phase and suppressed the Li-ion movement in the prepared SE.

Figures 7 and S5 show the SEM analysis of the $Li_{1+x}Al_{1+x}Si_{1-x}O_4$ ($x = 0-0.4$) pellets sintered at 800 °C for 18 h. It was found that conventional $LiAlSiO_4$ SE particles were not closely attached, leading to low-density electrolytes. As the *x* value increased, the porosity decreased, and the density of the pellet increased to 91%, which was conducive to the faster movement of Li ions.[51] Figure S4 shows a comparison of the ionic conductivities corresponding to the optimum sintering temperature, optimum sintering duration, and optimum $Li_{1+x}Al_{1+x}Si_{1-x}O_4$ ($x = 0-0.25$) composition. The room temperature ionic conductivity of the LASO pellet sintered at 800 °C was 2.11×10^{-6} S cm^{-1}, and the ionic conductivity after sintering for 18 h was 3.89×10^{-6} S cm^{-1}. With a change in the composition of the $Li_{1.25}Al_{1.25}Si_{0.75}O_4$ SE, the ionic conductivity increased to 1.07×10^{-5} S cm^{-1}, five times the conductivity of the pristine sample. After the *x* value increased, the density of the pellet increased to 91%, but still, the ionic conductivity of the SE is low. The lower density compared to the theoretical pellet density, nonuniform particle size, and shape are the main reasons for the low ionic conductivity. If we realize the pellet density of >98%, we can achieve higher ionic conductivity (>10^{-3} S cm^{-1}) in such SEs.

3.5. Electrochemical Performance of the Li//LASO//Li Symmetric Cell and the Li//LASO//LFP Solid-State Battery. Figure 8a illustrates the galvanostatic charge−discharge performance for the Li symmetric cell using $Li_{1+x}Al_{1+x}Si_{1-x}O_4$ ($x = 0.25$) as a SE. The current density of 0.1 mA cm^{-2} was applied during the Li-plating/stripping process, and the current direction of the cell was altered every 30 min. The initial overpotential of the Li-symmetric cell was 48 mV, but after a few cycles, the overpotential decreased due

https://doi.org/10.1021/acsami.3c15221
ACS Appl. Mater. Interfaces 2024, 16, 761−771

to smooth Li-ion transfer. After 500 cycles, there were no fluctuations and change in the cell performance, which implies that the SE can suppress dendrite formation for long cycle life. The SE was also tested at different current densities for the Li-plating/stripping process (Figure 8b). The overpotential of the cell was increased at a higher current density, but the cell still maintained a stable cycling performance at high rates. The addition of liquid electrolytes (LEs) enables a better ion transfer pathway and changes the particle−particle contact to the particle−LE contact.

Figure S5 shows the surface morphology of the LASO SE, which was studied to understand the contact loss of the cell. After 500 cycles, small cracks were formed on the surface of the LASO particles, and the volume expansion was the prime reason for crack formation. To further improve the lithiophilic nature of the SE by a protective coating layer over the SE surface is a good choice, which is being examined in our ongoing work.

Furthermore, the charge−discharge performance of the Li//$Li_{1+x}Al_{1+x}Si_{1-x}O_4$ (x = 0.25)//LFP cell was tested at a rate of 0.2 C rate. As shown in Figure 8c, the Li//LFP cell delivers initial charge and discharge capacities of about 109 and 94 mA h g^{-1}, respectively, with a corresponding Coulombic efficiency of 86%. The cell capacity is increased to 104 mA h g^{-1} due to the slow activation process. After 100 cycles, the cell rendered a discharge capacity of 101 mA h g^{-1}, which corresponds to 97% of its maximum reversible capacity (Figure 8d). Table 7 shows the capacity retention and capacity fade rate of the Li//$Li_{1+x}Al_{1+x}Si_{1-x}O_4$ (x = 0.25)//LFP cell. The major reason for the capacity loss is the Li-ion irreversibility and higher charge-transfer resistance across the electrode−electrolyte interface. Overall, the electrochemical performance is good, but the cell is not in a complete solid-state configuration. Therefore, we suggest further improving the contact area between the cathode active material and SE in all-state Li-ion batteries using a sintering aid and molten salt.

4. CONCLUSIONS

In this study, DFT was employed to determine the crystal structure and lattice parameters of LASO. The sol−gel method was used to prepare the LASO (x = 0−0.25) SE, and in the synthesis process, the sintering temperature, sintering duration, and doping composition were optimized. XRD results showed that below 700 °C, the LASO pellet contained the $LiAlO_2$ impurity phase. This impurity phase disappeared when higher sintering temperatures were used. The LASO pellet sintered at 800 °C had a higher ionic conductivity of 2.11 × 10^{-6} S cm^{-1} due to a decrease in the total resistance of the electrolyte. Furthermore, the unit cell volume of the SE pellet sintered at 800 °C for 18 h was larger, which had a positive effect on the electrochemical performance. To optimize the substitution composition of $Li_{1+x}Al_{1+x}Si_{1-x}O_4$ (x = 0−0.25), we increased the lithium (Li^+) concentration to increase the total ionic conductivity and relative density. Following the optimization, the $Li_{1.25}Al_{1.25}Si_{0.75}O_4$ SE had an ionic conductivity of 1.07 × 10^{-5} S cm^{-1}. The ionic conductivity of the electrolyte can be further increased by optimizing the particle size, refining the sintering process, and increasing the compactness of the pellet by applying a higher pressure during pellet formation. These measures could help realize an SE that can be used in practical cells.

ASSOCIATED CONTENT

Supporting Information

The Supporting Information is available free of charge at https://pubs.acs.org/doi/10.1021/acsami.3c15221.

Additional material characterization of MDS of the LASO electrolyte, FE-SEM images of the LASO particle, comparison of the ionic conductivity curve, FE-SEM images of $Li_{1.4}Al_{1.4}Si_{0.6}O_4$ electrolyte, and post-mortem FE-SEM images of the $Li_{1+x}Al_{1+x}Si_{1-x}O_4$ (x = 0.25) electrolyte (PDF)

AUTHOR INFORMATION

Corresponding Authors

Vanchiappan Aravindan − *Department of Chemistry, Indian Institute of Science Education and Research (IISER), Tirupati 517507, India;* orcid.org/0000-0003-1357-7717; Email: aravind.van@gmail.com

Sangho Park − *Department of Battery Engineering, Dongshin University, Jeollanam-do 58245, Republic of Korea;* Email: shpark@dsu.ac.kr

Sung June Cho − *Faculty of Chemical Engineering, Chonnam National University, Gwangju 500 757, Republic of Korea;* orcid.org/0000-0002-0030-9409; Email: sjcho@chonnam.ac.kr

Yun-Sung Lee − *Faculty of Chemical Engineering, Chonnam National University, Gwangju 500 757, Republic of Korea;* orcid.org/0000-0002-6676-2871; Email: leeys@chonnam.ac.kr

Authors

Je-Gwang Ryu − *Faculty of Chemical Engineering, Chonnam National University, Gwangju 500 757, Republic of Korea*

Ramkumar Balasubramaniam − *Faculty of Chemical Engineering, Chonnam National University, Gwangju 500 757, Republic of Korea*

Complete contact information is available at: https://pubs.acs.org/10.1021/acsami.3c15221

Author Contributions

J.-G.R. and R.B. conducted the conceptualization, data curation, investigation, visualization, writing−original draft, and writing—review and editing. V.A. performed the validation, supervision, and writing−review and editing. S.P. carried out the resource procurement, visualization, validation, and supervision. S.J.C. participated in the theoretical studies, methodology, validation, supervision, and draft manuscript preparation. Y.-S.L. accomplished the supervision, resource procurement, visualization, and project administration. All authors have given approval to the final version of the manuscript.

Notes

The authors declare no competing financial interest.

ACKNOWLEDGMENTS

This work was supported by a National Research Foundation (NRF) of Korea grant funded by the Korean government (Ministry of Science, ICT and Future Planning; no. 2021M3H4A1A04093047). V.A. acknowledges financial support from the Science and Engineering Research Board, a statutory body of DST, Govt. of India, through a Swarnajayanti Fellowship (SB/SJF/2020-21/12).

REFERENCES

(1) Zhang, X.; Li, Z.; Luo, L.; Fan, Y.; Du, Z. A review on thermal management of lithium-ion batteries for electric vehicles. *Energy.* **2022**, *238*, 121652.

(2) Ramkumar, B.; Yuvaraj, S.; Surendran, S.; Pandi, K.; Ramasamy, H. V.; Lee, Y.; Kalai Selvan, R. Synthesis and characterization of carbon coated $LiCo_{1/3}Ni_{1/3}Mn_{1/3}O_2$ and bio-mass derived graphene like porous carbon electrodes for aqueous Li-ion hybrid supercapacitor. *J. Phys. Chem. Solids* **2018**, *112*, 270−279.

(3) Lee, S. B.; Balasubramaniam, R. Double-shelled hybrid $MgFe_2O_4/Fe_2O_3$ hollow microspheres as a high-capacity anode for lithium-ion batteries. *J. Ind. Eng. Chem.* **2022**, *110*, 262−273.

(4) Chen, Y.; Jiang, Y.; Chi, S. S.; Woo, H. J.; Yu, K.; Ma, J.; Wang, J.; Wang, C.; Deng, Y. Understanding the lithium dendrites growth in garnet-based solid-state lithium metal batteries. *J. Power Sources* **2022**, *521*, 230921.

(5) Jenkins, R.; Snyder, R. L. Introduction to X-ray Powder Diffractometry. *Introduction to X-ray Powder Diffractometry*; Wiley, 1996.

(6) Kim, K. J.; Balaish, M.; Wadaguchi, M.; Kong, L.; Rupp, J. L. M. Solid-State Li−Metal Batteries: Challenges and Horizons of Oxide and Sulfide Solid Electrolytes and Their Interfaces. *Adv. Energy Mater.* **2021**, *11* (1), 2170002.

(7) Jonson, R. A.; McGinn, P. J. Tape casting and sintering of $Li_7La_3Zr_{1.75}Nb_{0.25}Al_{0.1}O_{12}$ with Li_3BO_3 additions. *Solid State Ionics* **2018**, *323*, 49−55.

(8) Ramkumar, B.; So-young, K.; Chan-woo, N.; Aravindan, V.; Yun-Sung, L. $LiBO_2$-modified $LiCoO_2$ as an efficient cathode with garnet framework $Li_{6.75}La_3Zr_{1.75}Nb_{0.25}O_{12}$ electrolyte toward building all-solid-state lithium battery for high-temperature operation. *Electrochim. Acta* **2020**, *359*, 136955.

(9) Balasubramaniam, R.; Nam, C.; Aravindan, V.; Eum, D.; Kang, K.; Lee, Y. Interfacial Engineering in a Cathode Composite Based on Garnet-Type Solid-State Li-Ion Battery with High Voltage Cycling. *ChemElectroChem* **2021**, *8* (3), 570−576.

(10) Manthiram, A.; Yu, X.; Wang, S. Lithium battery chemistries enabled by solid-state electrolytes. *Nat. Rev. Mater.* **2017**, *2* (4), 16103−16116.

(11) Li, S.; Zhang, S. Q.; Shen, L.; Liu, Q.; Ma, J. B.; Lv, W.; He, Y. B.; Yang, Q. H. Progress and Perspective of Ceramic/Polymer Composite Solid Electrolytes for Lithium Batteries. *Adv. Sci.* **2020**, *7* (5), 1903088.

(12) Balasubramaniam, R.; Nam, C. W.; Aravindan, V.; Seol, J. C.; Ajeya, K. V.; Jung, H. Y.; Lee, Y. S. Composite Solid Electrolyte for High Voltage Solid-State Li-Metal Battery. *ChemElectroChem* **2022**, *9* (14), No. e202200317.

(13) Seol, J. C.; Balasubramaniam, R.; Aravindan, V.; Thangavel, R.; Lee, Y. S. Ameliorating the electrode/electrolyte interface compatibility in Li-ion solid-state batteries with plasticizer. *J. Alloys Compd.* **2022**, *927*, 167077.

(14) Chen, X.; Guan, Z.; Chu, F.; Xue, Z.; Wu, F.; Yu, Y. Air-stable inorganic solid-state electrolytes for high energy density lithium batteries: Challenges, strategies, and prospects. *InfoMat* **2022**, *4* (1), No. e12248.

(15) Jonderian, A.; McCalla, E. The role of metal substitutions in the development of Li batteries, part II: Solid electrolytes. *Mater. Adv.* **2021**, *2* (9), 2846−2875.

(16) Beaupain, J. P.; Waetzig, K.; Otto, S. K.; Henss, A.; Janek, J.; Malaki, M.; Pokle, A.; Muller, J.; Butz, B.; Volz, K.; Kusnezoff, M.; Michaelis, A. Reaction of $Li_{1.3}Al_{0.3}Ti_{1.7}(PO_4)_3$ and $LiNi_{0.6}Co_{0.2}Mn_{0.2}O_2$ in Co-Sintered Composite Cathodes for Solid-State Batteries. *ACS Appl. Mater. Interfaces* **2021**, *13* (40), 47488−47498.

(17) Wu, J. F.; Chen, E. Y.; Yu, Y.; Liu, L.; Wu, Y.; Pang, W. K.; Peterson, V. K.; Guo, X. Gallium-doped $Li_7La_3Zr_2O_{12}$ garnet-type electrolytes with high lithium-ion conductivity. *ACS Appl. Mater. Interfaces* **2017**, *9* (2), 1542−1552.

(18) Lu, Y.; Meng, X.; Alonso, J. A.; Fernández-Díaz, M. T.; Sun, C. Effects of Fluorine Doping on Structural and Electrochemical Properties of $Li_{6.25}Ga_{0.25}La_3Zr_2O_{12}$ as Electrolytes for Solid-State Lithium Batteries. *ACS Appl. Mater. Interfaces* **2019**, *11* (2), 2042−2049.

(19) Wu, J. F.; Pu, B. W.; Wang, D.; Shi, S. Q.; Zhao, N.; Guo, X.; Guo, X. In Situ Formed Shields Enabling Li_2CO_3-Free Solid Electrolytes: A New Route to Uncover the Intrinsici Lithiophilicity of Garnet Electrolytes for Dendrite-Free Li-Metal Batteries. *ACS Appl. Mater. Interfaces* **2019**, *11*, 898−905.

(20) Ramkumar, B.; Aravindan, V.; Ramasamy, H.; Ajeya, K. V.; Ryu, J. G.; Jung, H. Y.; Lee, Y. S. Ternary metal oxide filled PEO-based polymer electrolyte for solid-state lithium metal battery: The role of filler particle size. *Solid State Sci.* **2022**, *132*, 106958.

(21) Choi, H. J.; Kim, S. Y.; Gong, M. K.; Vignesh, H.; Aravindan, V.; Lee, Y. G.; Lee, Y. S. Tailored perovskite $Li_{0.33}La_{0.56}TiO_3$ via an adipic acid-assisted solution process: A promising solid electrolyte for lithium batteries. *J. Alloys Compd.* **2017**, *729*, 338−343.

(22) Wu, X. M.; Li, X. H.; Wang, S. W.; Wang, Z.; Zhang, Y. H.; Xu, M. F.; He, Z. Q. Preparation and characterization of lithium-ion-conductive $Li_{1.3}Al_{0.3}Ti_{1.7}(PO_4)_3$ thin films by the solution deposition. *Thin Solid Films* **2003**, *425* (1−2), 103−107.

(23) Paolella, A.; Zhu, W.; Xu, G. L.; La Monaca, A.; Savoie, S.; Girard, G.; Vijh, A.; Demers, H.; Perea, A.; Delaporte, N.; Guerfi, A.; Liu, X.; Ren, Y.; Sun, C. J.; Lu, J.; Amine, K.; Zaghib, K. Understanding the Reactivity of a Thin $Li_{1.5}Al_{0.5}Ge_{1.5}(PO_4)_3$ Solid-State Electrolyte toward Metallic Lithium Anode. *Adv. Energy Mater.* **2020**, *10* (32), 1−7.

(24) Hartmann, P.; Leichtweiss, T.; Busche, M. R.; Schneider, M.; Reich, M.; Sann, J.; Adelhelm, P.; Janek, J. Degradation of NASICON-type materials in contact with lithium metal: Formation of mixed conducting interphases (MCI) on solid electrolytes. *J. Phys. Chem. C* **2013**, *117* (41), 21064−21074.

(25) Sharafi, A.; Yu, S.; Naguib, M.; Lee, M.; Ma, C.; Meyer, H. M.; Nanda, J.; Chi, M.; Siegel, D. J.; Sakamoto, J. Impact of air exposure and surface chemistry on Li-$Li_7La_3Zr_2O_{12}$ interfacial resistance. *J. Mater. Chem. A* **2017**, *5* (26), 13475−13487.

(26) Huo, H.; Luo, J.; Thangadurai, V.; Guo, X.; Nan, C. W.; Sun, X. Li_2CO_3: A Critical Issue for Developing Solid Garnet Batteries. *ACS Energy Lett.* **2020**, *5* (1), 252−262.

(27) Yaroshevsky, A. A. Abundances of chemical elements in the Earth's crust. *Geochem. Int.* **2006**, *44* (1), 48−55.

(28) Fleischer, M. The abundance and distribution of the chemical elements in the earth's crust. *J. Chem. Educ.* **1954**, *31* (9), 446−455.

(29) Sheil, R.; Perng, Y. C.; Mars, J.; Cho, J.; Dunn, B.; Toney, M. F.; Chang, J. P. Synthesis and Crystallization of Atomic Layer Deposition β-Eucryptite $LiAlSiO_4$Thin-Film Solid Electrolytes. *ACS Appl. Mater. Interfaces* **2020**, *12* (51), 56935−56942.

(30) Stebbins, J. F.; Xu, Z. NMR evidence for excess non-bridging oxygen in an aluminosilicate glass. *Nature* **1997**, *390* (6655), 60−62.

(31) Zhao, Y.; Zhang, X.; Chen, X.; Li, W.; Li, Z.; Chen, M.; Sun, W.; Zhao, J.; Li, Y. All-solid-state electrochromic devices based on the $LiAlSiO_4$ electrolyte. *Mater. Lett.* **2021**, *292*, 129592.

(32) Wu, Y.; Li, X.; Yan, G.; Wang, Z.; Guo, H.; Ke, Y.; Wu, L.; Fu, H.; Wang, J. Incorporating multifunctional $LiAlSiO_4$ into polyethylene oxide for high-performance solid-state lithium batteries. *J. Energy Chem.* **2021**, *53*, 116−123.

(33) Giannozzi, P.; Baroni, S.; Bonini, N.; Calandra, M.; Car, R.; Cavazzoni, C.; Ceresoli, D.; Chiarotti, G. L.; Cococcioni, M.; Dabo, I.; Dal Corso, A.; de Gironcoli, S.; Fabris, S.; Fratesi, G.; Gebauer, R.; Gerstmann, U.; Gougoussis, C.; Kokalj, A.; Lazzeri, M.; Martin-Samos, L.; Marzari, N.; Mauri, F.; Mazzarello, R.; Paolini, S.; Pasquarello, A.; Paulatto, L.; Sbraccia, C.; Scandolo, S.; Sclauzero, G.; Seitsonen, A. P.; Smogunov, A.; Umari, P.; Wentzcovitch, R. M. QUANTUM ESPRESSO: A modular and open-source software project for quantum simulations of materials. *J. Phys.: Condens. Matter* **2009**, *21* (39), 395502.

(34) Ross, S.; Welsch, A. M.; Behrens, H. Lithium conductivity in glasses of the Li_2O-Al_2O_3-SiO_2 system. *Phys. Chem. Chem. Phys.* **2015**, *17* (1), 465−474.

https://doi.org/10.1021/acsami.3c15221
ACS Appl. Mater. Interfaces 2024, 16, 761−771

(35) Pang, M. C.; Marinescu, M.; Wang, H.; Offer, G. Mechanical behaviour of inorganic solid-state batteries: can we model the ionic mobility in the electrolyte with Nernst-Einstein's relation? *Phys. Chem. Chem. Phys.* **2021**, *23* (48), 27159−27170.
(36) Kobayashi, K.; Nagai, Y.; Itakura, M.; Shiga, M. Self-learning hybrid Monte Carlo method for isothermal-isobaric ensemble: Application to liquid silica. *J. Chem. Phys.* **2021**, *155* (3), 034106.
(37) Huang, Y.; Kang, J.; Goddard, W. A.; Wang, L. W. Density functional theory based neural network force fields from energy decompositions. *Phys. Rev. B* **2019**, *99*, 064103.
(38) Thompson, A. P.; Aktulga, H. M.; Berger, R.; Bolintineanu, D. S.; Brown, W. M.; Crozier, P. S.; in 't Veld, P. J.; Kohlmeyer, A.; Moore, S. G.; Nguyen, T. D.; Shan, R.; Stevens, M. J.; Tranchida, J.; Trott, C.; Plimpton, S. J. LAMMPS - a flexible simulation tool for particle-based materials modeling at the atomic, meso, and continuum scales. *Comput. Phys. Commun.* **2022**, *271*, 108171.
(39) Davaasuren, B.; Tietz, F. Impact of sintering temperature on phase formation, microstructure, crystallinity and ionic conductivity of $Li_{1.5}Al_{0.5}Ti_{1.5}(PO_4)_3$. *Solid State Ionics* **2019**, *338*, 144−152.
(40) Irshad, M.; Rafique, M.; Tabish, A. N.; Ghaffar, A.; Shakeel, A.; Siraj, K.; Ain, Q. U.; Raza, R.; Assiri, M. A.; Imran, M. Influence of Sintering Temperature on the Structural, Morphological, and Electrochemical Properties of NiO-YSZ Anode Synthesized by the Autocombustion Route. *Metals* **2022**, *12* (2), 219.
(41) Xu, H.; Heaney, P. J.; Beall, G. H. Phase transitions induced by solid solution in stuffed derivatives of quartz: A powder synchrotron XRD study of the $LiAlSiO_4$-SiO_2 join. *Am. Mineral.* **2000**, *85* (7−8), 971−979.
(42) Wiedemann, D.; Nakhal, S.; Rahn, J.; Witt, E.; Islam, M. M.; Zander, S.; Heitjans, P.; Schmidt, H.; Bredow, T.; Wilkening, M.; Lerch, M. Unravelling Ultraslow Lithium-Ion Diffusion in γ-$LiAlO_2$: Experiments with Tracers, Neutrons, and Charge Carriers. *Chem. Mater.* **2016**, *28* (3), 915−924.
(43) He, X.; Bai, Q.; Liu, Y.; Nolan, A. M.; Ling, C.; Mo, Y. Crystal Structural Framework of Lithium Super-Ionic Conductors. *Adv. Energy Mater.* **2019**, *9* (43), 1−12.
(44) Moradkhani, A.; Baharvandi, H.; Naserifar, A. Effect of sintering temperature on the grain size and mechanical properties of Al_2O_3-SiC nanocomposites. *J. Korean Ceram. Soc.* **2019**, *56* (3), 256−268.
(45) Zöllner, D. Impact of a strong temperature gradient on grain growth in films. *Modell. Simul. Mater. Sci. Eng.* **2022**, *30* (2), 025010.
(46) Fourquet, J. L.; Duroy, H.; Crosnier-Lopez, M. P. Structural and Microstructural Studies of the Series $La_{2/3-x}$ $Li_{3x1/3-2x}$ TiO_3. *J. Solid State Chem.* **1996**, *127* (2), 283−294.
(47) Kittel, C.; Hellwarth, R. W. Introduction to Solid State Physics. *Phys. Today* **1957**, *10* (6), 43−44.
(48) Le Bail, A. Structure determination of $NaPbFe_2F_9$ by X-ray powder diffraction. *J. Solid State Chem.* **1989**, *83* (2), 267−271.
(49) Perdew, J. P.; Burke, K.; Ernzerhof, M. Generalized gradient approximation made simple. *Phys. Rev. Lett.* **1996**, *77* (18), 3865−3868.
(50) Grimme, S.; Antony, J.; Ehrlich, S.; Krieg, H. A consistent and accurate ab initio parametrization of density functional dispersion correction (DFT-D) for the 94 elements H-Pu. *J. Chem. Phys.* **2010**, *132* (15), 154104.
(51) Zhang, J.; Zhao, Y.; Xu, H.; Zelinskas, M. V.; Wang, L.; Wang, Y.; Uchida, T. Pressure-induced amorphization and phase transformations in β-$LiAlSiO_4$. *Chem. Mater.* **2005**, *17* (11), 2817−2824.

https://doi.org/10.1021/acsami.3c15221
ACS Appl. Mater. Interfaces 2024, 16, 761−771